論文 / 著書情報
Article / Book Information

Title	Ultra-compact microring optical isolator using an aluminum-substituted cobalt ferrite thin film
Authors	Kotaro Sato, Makoto Okano, Yuya Shoji
Citation	Optica, Vol. 11, No. 6, pp. 889-895
Pub. date	2024, 6
Copyright	(c) 2024 Optica Publishing Group. Users may use, reuse, and build upon the article, or use the article for text or data mining, so long as such uses are for non-commercial purposes and appropriate attribution is maintained. All other rights are reserved.
DOI	http://dx.doi.org/10.1364/OPTICA.511956

OPTICA

Ultra-compact microring optical isolator using an aluminum-substituted cobalt ferrite thin film

KOTARO SATO,[1] MAKOTO OKANO,[2] AND YUYA SHOJI[1,3,*]

[1] Department of Electrical and Electronic Engineering, School of Engineering, Tokyo Institute of Technology, 2-12-1, Ookayama, Meguro-ku, Tokyo 152-8550, Japan
[2] National Institute of Advanced Industrial Science and Technology (AIST), Ibaraki 305-8568, Japan
[3] Laboratory for Future Interdisciplinary Research of Science and Technology, Tokyo Institute of Technology, 2-12-1, Ookayama, Meguro-ku, Tokyo 152-8550, Japan
*shoji@ee.e.titech.ac.jp

Received 9 November 2023; revised 5 June 2024; accepted 5 June 2024; published 20 June 2024

Yttrium iron garnets, which are typically used as magneto-optical isolators, are not suitable for monolithic integration with photonic circuits. We experimentally demonstrated an ultracompact microring optical isolator using an aluminum-substituted cobalt ferrite (CAFO) thin film directly deposited on silicon waveguides. The device footprint was only 43 × 71 μm^2. The isolator can operate without an external magnet owing to the strong remanent magnetization of the CAFO film and achieved a maximum isolation ratio of 24.7 dB at a wavelength of 1545.7 nm. Our study could facilitate integration of nonreciprocal photonic devices on Si platforms.

https://doi.org/10.1364/OPTICA.511956

1. INTRODUCTION

Optical isolators are nonreciprocal devices that allow the propagation of light in only one direction while preventing light from propagating in the opposite direction, which is indispensable for protecting optically active elements from backward reflections and stabilizing their operation. A plethora of approaches to realize integrated optical isolators by breaking the Lorentz reciprocity [1] have been reported using nonlinear [2–6], electro-optical [7–11], and acousto-optical effects [12–16]. Some of them are based on a directionally dependent spatio-temporal modulation first proposed in [11] taking advantage of the easy-to-fabricate structure, whereas they suffer from a long interaction length and need of power consumption. On the other hand, integrated optical isolators based on magneto-optical (MO) effects [17–26] are the most promising because of their simple structure and purely passive operation. The main challenge is how to integrate the materials.

Magnetized MO materials exhibit first-order MO effects and non-reciprocal light propagation. Garnet ferrites, such as bismuth-substituted yttrium iron garnet (Bi:YIG) and cerium-substituted yttrium iron garnet (Ce:YIG), have a large MO effect and low optical absorption in the telecommunication wavelength region [27,28]. However, the growth of single-crystalline MO garnets on semiconductors is extremely difficult because of the lattice and thermal expansion mismatch. In addition, these garnets require an external magnetic field to maintain magnetization using a permanent magnet or electromagnet, which increases the device size. There are two approaches to integrating Ce: YIG on a silicon photonics platform: bonding and deposition. Direct bonding between an epitaxially grown Ce:YIG film on a gadolinium gallium garnet (GGG) substrate and a silicon-on-insulator (SOI) wafer was realized using a surface-activated direct bonding technique [24]. This method allows the use of good-quality Ce:YIG films, but requires a large chip area, and a thick GGG substrate remains; thus, the fabrication process after bonding is complicated. Using an yttrium iron garnet (YIG) seed layer, a polycrystalline Ce:YIG film was deposited on the SOI [29]. The polycrystalline Ce:YIG film exhibits a lesser figure of merit than the single-crystalline Ce:YIG film.

Cobalt ferrite ($CoFe_2O_4$: CFO), a spinel ferrite, has a Faraday rotation coefficient under saturated magnetization five times larger than that of Ce:YIG and enables a compact MO isolator. Serrano-Núñez *et al*. developed a silicon optical isolator using a monolithically integrated CFO film [18]. According to the report, the polycrystalline CFO film deposited on Si showed a large Faraday rotation coefficient (θ_F) of 25,600 deg/cm at 1550 nm wavelength, while high material loss of 3.4 dB/μm was a challenge [30]. Therefore, the figure of merit between the MO effect and the loss was much lower than that of Ce:YIG. However, CFO possesses a strong remanent magnetization and coercive force, which means that a more compact structure is possible without the need for external permanent magnets.

In this paper, we focus on aluminum-substituted cobalt ferrite, which can reduce material loss by sacrificing a slight degradation of θ_F. $CoAl_{0.57}Fe_{1.43}O_4$ (CAFO) is expected to have the highest advantages among reported compositions [31]. The sputtering method was employed for the deposition of the CAFO. Using the sputtering method, films of the same composition as the target material are easily formed, the energy of the film particles is large, adhesion is strong, the film thickness can be controlled with high accuracy only by time, and a uniform film can be formed even on a large surface area, while the deposition speed is slow. The characteristics of the CAFO film depend on the sputtering conditions and the buffer layer. We investigated the use of two buffer layers, magnesium oxide (MgO) and zinc oxide (ZnO), to fabricate highly oriented CAFO films. The low optical absorption and refractive index of 1.71 of MgO in communication bands make it suitable for integration in optical waveguides [32,33]. ZnO has a hexagonal wurtzite crystalline structure and is a promising material for buffer layers in the selective growth of CAFO films. (0001)-oriented ZnO can be deposited on Si (100), and (111)-oriented CFO can be deposited on ZnO (0001) [34,35]. The (111) single-oriented CFO film may exhibit a magnetic easy axis in the in-plane direction with a large remanent magnetization, which is potentially useful for TM-mode optical isolators using a CAFO film [36]. Finally, we fabricated a microring resonator (MRR)-based MO isolator with a compact device footprint. The CAFO/MgO was deposited on the Si waveguide, where the over cladding was partially opened. Efficient resonant wavelength shifts due to the MO effect and a high isolation ratio (IR) were successfully obtained.

2. PREPARATION OF ALUMINUM-SUBSTITUTED COBALT FERRITE

CAFO, MgO, and ZnO were deposited on a 1.5 × 1.5 cm^2 Si (100) substrate using multi-target radio frequency (RF) magnetron sputtering equipment. The Si (100) substrate was dipped in diluted hydrogen fluoride (DHF) for 30 s to remove the native oxide layer and cleaned with acetone using ultrasonication for 5 min. The MgO buffer layer was deposited using a MgO target at a substrate temperature of 600°C, chamber pressure of 3 Pa, RF power of 80 W, and argon (Ar) gas flow of 20 sccm. Under these conditions, highly oriented MgO (100) layers with a thickness of 20 nm were formed on the Si (100) substrate [30]. The ZnO buffer layer was deposited using a ZnO target at a substrate temperature of 600°C, chamber pressure of 3 Pa, RF power of 80 W, and Ar gas flow of 20 sccm. Under these conditions, a highly oriented ZnO (0001) layer with a thickness of 78 nm was formed on a Si (100) substrate. The CAFO films were deposited on these buffer layers using a CAFO target under the following conditions: the CAFO on the MgO buffer layer was deposited at a substrate temperature of 750°C, chamber pressure of 1 Pa, RF power of 200 W, and Ar gas flow of 20 sccm. The CAFO on the ZnO buffer layer was deposited at a substrate temperature of 750°C, chamber pressure of 1 Pa, RF power of 180 W, and Ar gas flow of 20 sccm. In addition, CAFO was directly deposited onto Si without any buffer layer at a substrate temperature of 750°C, chamber pressure of 1 Pa, RF power of 180 W, and Ar gas flow of 20 sccm.

The CAFO properties were evaluated using the following equipment. The crystallinity of the deposited CAFO film was characterized by the θ-2θ scans of standard Cu-Kα X-ray diffraction (XRD). The film thicknesses were measured using scanning electron microscopy (SEM).

The MO effects were measured using Faraday rotation (FR) characterization with light penetrating the film vertically under an out-of-plane external magnetic field at room temperature. Magnetic hysteresis loops were measured using a vibrating sample magnetometer (VSM) at room temperature. The material loss was evaluated from the transmittances of the Si waveguides with different CAFO cladding lengths along the light propagation direction.

Figure 1(a) shows the XRD patterns of the CAFO/MgO/Si, CAFO/ZnO/Si, and CAFO/Si films. The XRD pattern of the deposited CAFO/MgO/Si film shows a peak of 2θ around 43.6°, corresponding to a (400) miller index of CAFO and (200) miller index of MgO. Almost all the single crystals of CAFO (100) were obtained using the MgO buffer layer. The XRD pattern of the deposited CAFO/ZnO/Si film shows peaks of 2θ around 18.6°, 34.6°, 37.5°, and 57.8°, corresponding to (111), (222), and (333) miller indices of CAFO and (0002) miller index of ZnO. Almost all the single crystals of CAFO (111) were obtained using the ZnO buffer layer. The XRD pattern of the deposited CAFO/Si film shows a small peak of intensity of 2θ around 35.9°, corresponding to a (311) miller index of CAFO. A CAFO film with poor orientation was confirmed without using a buffer layer. Single-crystal orientation of MO materials is important in photonic integrated circuits (PICs) to avoid absorption loss and optical scattering arising from the grain boundaries of multiplane structures. Using buffer layers, highly oriented CAFO films can be deposited, making them suitable for low-loss MO materials.

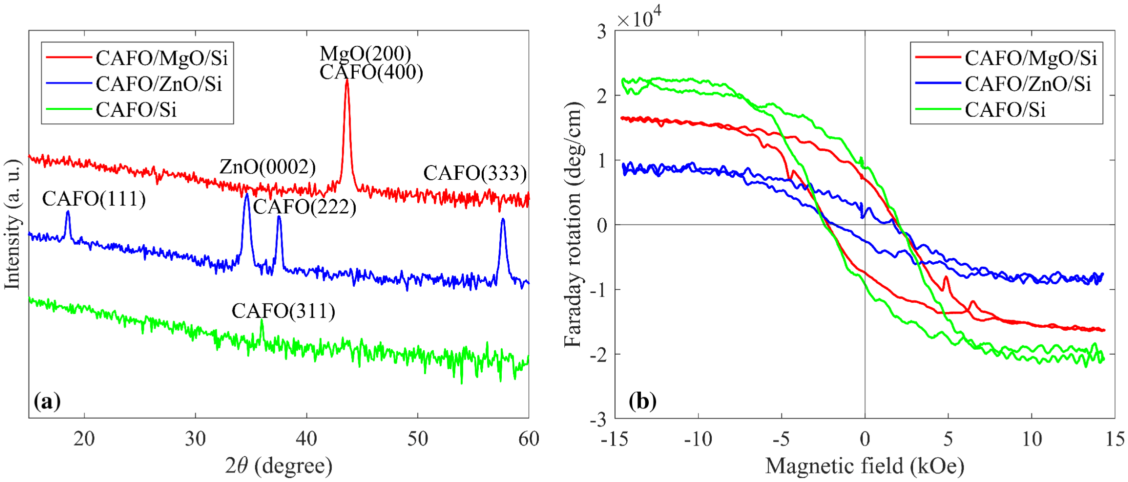

Fig. 1. (a) XRD patterns of CAFO/MgO/Si, CAFO/ZnO/Si, and CAFO/Si. (b) Room temperature Faraday rotation hysteresis loops of CAFO/MgO/Si, CAFO/ZnO/Si, and CAFO/Si.

The measured FR coefficients θ_F of hysteresis loops of CAFO films at a wavelength of 1550 nm are plotted in Fig. 1(b). The θ_F of the Si substrate, the MgO buffer layer, and the ZnO buffer layer were subtracted from the original data. The thickness of each film was measured using SEM, and the rotation angle was divided by the film thickness. The θ_F of the CAFO/Si film reached $-22{,}000$ deg/cm at the saturation, which was the largest FR measured. The θ_F of the CAFO/MgO/Si and the CAFO/ZnO/Si films reached $-15{,}000$ deg/cm and $-9{,}000$ deg/cm, respectively. The maximum θ_F of CAFO film was slightly smaller than 25,600 deg/cm with CFO in our previous work [30]. The reason for this is the substitution of Al. The negative loops are consistent with those reported by Suzuki *et al.* and do not affect the performance of the optical isolator [31].

Next, we evaluated the magnetic anisotropy. Figures 2(a)–2(c) show the magnetic hysteresis loops of the CAFO/MgO/Si film, both in-plane and out-of-plane, obtained using VSM at room temperature. Here, we define the squareness ratio of the remanence magnetization M_r and saturation magnetization M_s. In-plane squareness ratios of CAFO/MgO/Si, CAFO/ZnO/Si, and CAFO/Si films are 29%, 49%, and 60%, respectively. The CAFO/MgO/Si film exhibited an out-of-plane-oriented easy axis, whereas the CAFO/ZnO/Si and CAFO/Si films exhibited an in-plane-oriented easy axis. The in-plane easy axis, that is, a large in-plane squareness ratio, is suitable for the MO effect in the TM mode when the material is placed in the upper cladding layer. Similarly, the out-of-plane easy axis is suitable for the MO effect in the TE mode when the material is placed in the side cladding layer. However, the CAFO/MgO/Si film may have an in-plane-oriented easy axis when deposited at a low substrate temperature for sputtering [30].

To evaluate material loss, CAFO/MgO, CAFO/ZnO, and CAFO films were deposited on Si waveguides with different window lengths. Figures 2(d)–2(f) show the plots of the transmittances of the CAFO/MgO/Si, CAFO/ZnO/Si, and CAFO/Si waveguides at a wavelength of 1550 nm as a function of the window length. The propagation losses were determined to be 0.40 dB/μm, 0.36 dB/μm, and 3.48 dB/μm for the CAFO/MgO/Si, CAFO/ZnO/Si, and CAFO/Si waveguides from the slope calculated by linear approximation, respectively. The material loss of the CAFO (α_{CAFO}) can be inferred from its confinement factor (Γ_{CAFO}) in the waveguide. Based on the cross-sectional dimensions of the waveguide by SEM, $\Gamma_{\mathrm{CAFO\ on\ MgO}} = 45.3\%$, $\Gamma_{\mathrm{CAFO\ on\ ZnO}} = 39.6\%$, and $\Gamma_{\mathrm{CAFO\ on\ Si}} = 57.8\%$ were calculated with a mode solver based on the finite element method (Cybernet RSoft FemSIM). Therefore, $\alpha_{\mathrm{CAFO\ on\ MgO}}$, $\alpha_{\mathrm{CAFO\ on\ ZnO}}$, and $\alpha_{\mathrm{CAFO\ on\ Si}}$ were determined to be 0.83 dB/μm, 0.92 dB/μm, and 6.02 dB/μm, respectively. $\alpha_{\mathrm{CAFO\ on\ MgO}}$ and $\alpha_{\mathrm{CAFO\ on\ ZnO}}$ are lower than that of CFO [31]. However, $\alpha_{\mathrm{CAFO\ on\ Si}}$ was higher, probably because of its low crystal orientation.

The figure of merit (FoM) is used as an indicator to compare the performance of the MO materials. Because optical isolator operation without applying an external magnetic field is assumed in this study, the remanent FoM (°/dB) is defined as

$$\mathrm{FoM}_r = \left| \frac{\theta_F}{\alpha} \frac{M_r}{M_s} \right|, \tag{1}$$

where M_r/M_s is the in-plane square ratio of the CAFO film. Table 1 shows the characteristics of the CAFO films deposited with and without buffer layers as well as CFO and Ce:YIG in previous works. The CAFO/MgO/Si film exhibits the highest remanent FoM. The FoM of CAFO is much lower than that of Ce:YIG. However, FoM is independent from propagation length and its large Faraday rotation has an impact on the device size. In addition, Ce:YIG requires an external magnetic field integrating a permanent magnet.

3. DEVICE STRUCTURE AND FABRICATION

A schematic diagram of the device structure is shown in Fig. 3(a). An MRR of 440-nm-wide and 220-nm-thick Si ($n = 3.48$)

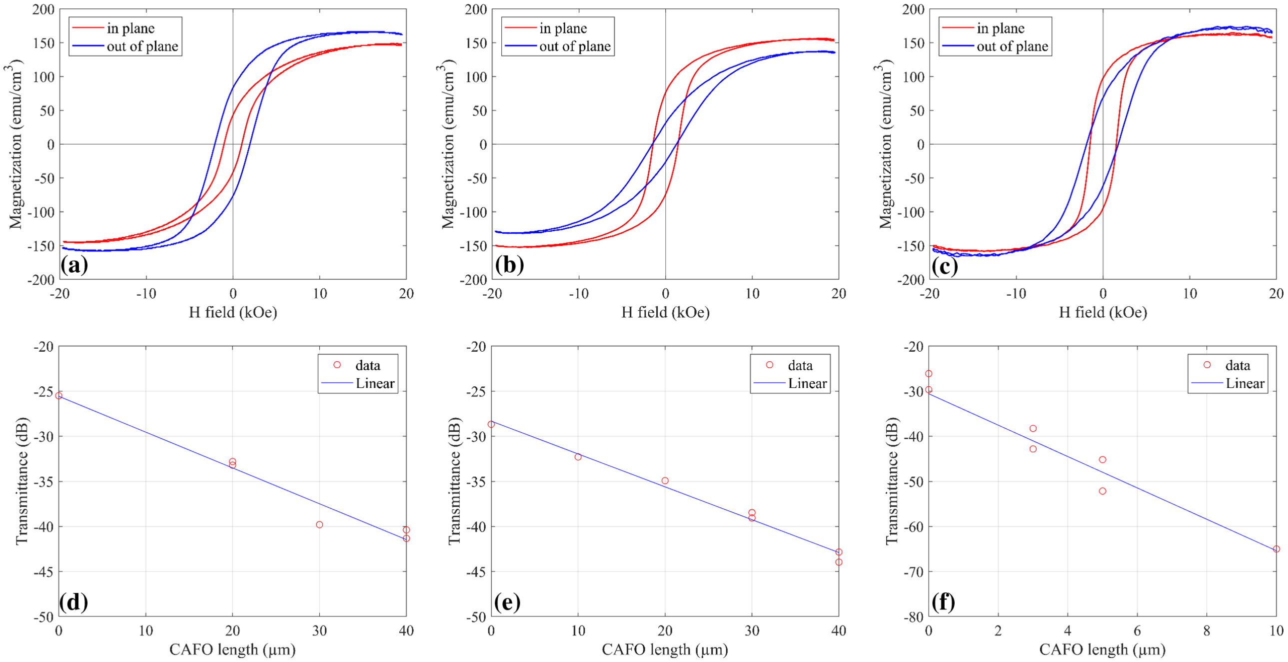

Fig. 2. In-plane and out-of-plane room temperature magnetization hysteresis loops of (a) CAFO/MgO/Si, (b) CAFO/ZnO/Si, and (c) CAFO/Si. The transmission loss of (d) CAFO/MgO/Si, (e) CAFO/ZnO/Si, and (f) CAFO/Si waveguide as a function of its length.

Table 1. Optical and Magnetic Properties of CAFO, CFO, Ce:YIG Films Deposited on Each Buffer Layer at a Wavelength of 1550 nm[a]

Material	CAFO			CFO [30]	Ce:YIG [24]
Buffer layer	**MgO**	**ZnO**	**None**	**MgO**	**None**
θ_F (deg/cm)	−15,000	−9,000	−2,2000	25,600	−4,500
α (dB/μm)	0.83	0.92	6.02	3.4	0.006
$\frac{M_r}{M_s}$	0.29	0.49	0.6	0.54	~ 0
FoM (deg/dB)	1.8	0.98	0.37	0.75	75
FoM_r (deg/dB)	0.52	0.42	0.22	0.40	-

[a] FoM and FoM_r are at the saturated and remanent magnetizations, respectively.

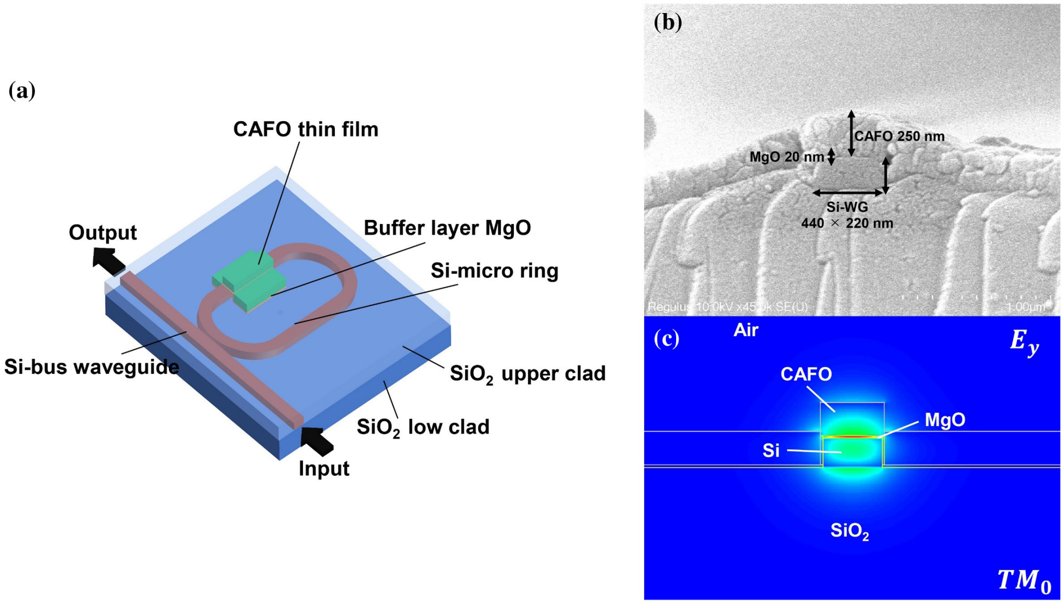

Fig. 3. (a) Schematic of the MRR isolator. (b) Cross-sectional SEM image of CAFO/MgO/Si waveguide. (c) Simulated E_y field distribution of the fundamental TM mode.

waveguides was patterned on a 3-μm-thick SiO$_2$ ($n = 1.444$) substrate. The bending radius was 20 μm, the length of the straight section in MRR was 30 μm, and the gap between the bus-line waveguide and the ring resonator was 200 nm. A silica layer of 2-μm thickness was deposited as upper cladding, where a window region was opened in one straight section. CAFO (250 nm)/MgO (20 nm) was deposited on Si at the window region to form a MO waveguide with an interaction length (L_{MO}) of 25 μm. The ring radius, gap between the bus-line waveguide and ring resonator, and L_{MO} were designed to satisfy the critical coupling conditions for the total internal loss, as described below. Owing to the thick silica layer, the waveguide optical mode interacted with the CAFO film only in the window region. When the CAFO film was magnetized in-plane and perpendicular to the direction of propagating light, the CAFO remnant magnetization induced nonreciprocal phase-shift effects (NRPS) of the TM mode by the MO effect. Figure 3(b) shows a cross-sectional view of the window region of the fabricated device as observed in SEM. Figure 3(c) shows the simulated modal profile for the actual dimensions. The NRPS of the TM mode can be calculated as

$$\text{NRPS}_{\text{TM}} = \frac{2\omega\varepsilon_0}{P} \iint \text{Re}\left(j\gamma E_y^* E_z\right) \mathrm{d}x\mathrm{d}y, \tag{2}$$

where ω is the angular frequency, ε_0 is the vacuum dielectric constant, P is the power flux along the z-axis, γ is the off-diagonal components of the permittivity tensor of the MO material, and E_y, E_z are the electric field components along the y and z directions. Considering in-plane remanent θ_F of CAFO film (−4,350 deg/cm) the simulated NRPS is 6.1 rad/mm.

The intensity transmission factor of the ring resonator can be given by

$$T = \frac{a^2 - 2ta\cos\beta L + t^2}{1 - 2ta\cos\beta L + (ta)^2}, \tag{3}$$

where a is the round-trip transmittance, which depends mainly on the MO material loss and the bending loss of the waveguide. t is the power transmission in the coupling region, which can be adjusted by varying the gap between the bus-line and ring waveguides. When the power loss inside the ring is equal to the coupled power, that is, $a = t$, T decreases to zero at the resonant phase. This is known as the critical coupling condition of the resonator, in which all resonant light is eventually dissipated inside the ring. To obtain a large isolation rate (IR), a design satisfying the critical coupling condition is required to obtain a large IR value. The bending loss is negligibly small at a ring radius $r \geq 20$ μm, so the ring radius was set at 20 μm. For L_{MO} of 25 μm and ring and waveguide gap of 200 nm, the critical coupling condition ($a \approx t$) would be satisfied.

Figure 4 shows the fabrication process flow of the device. The ring resonator and bus-line waveguide were fabricated on

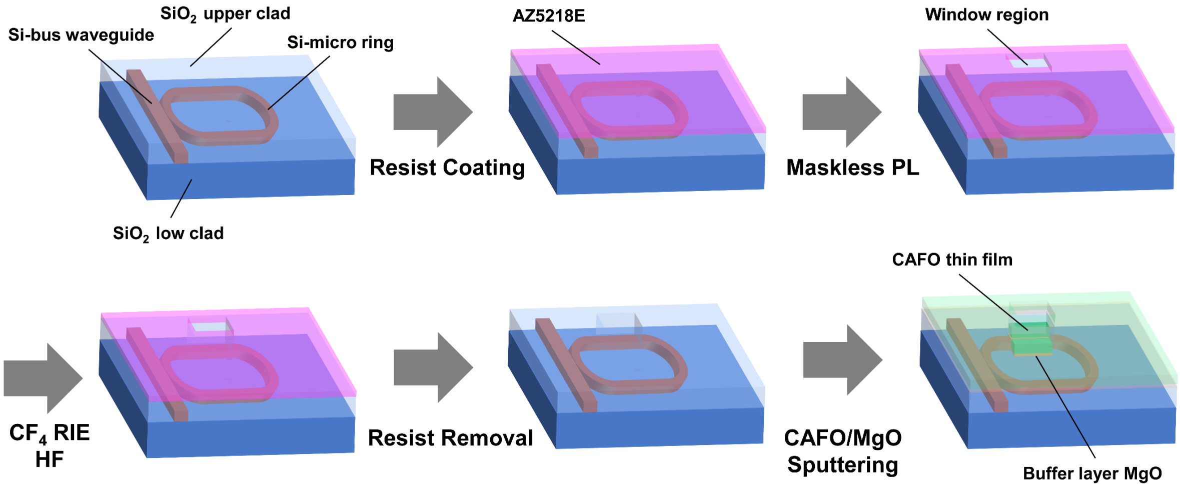

Fig. 4. Fabrication process of MRR optical isolator.

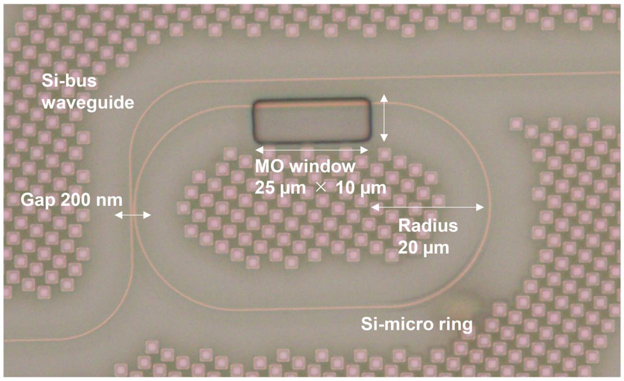

Fig. 5. Optical microscopic picture of the fabricated device before CAFO deposition.

silicon-on-insulator (SOI) wafers by using a CMOS-compatible process [37]. It had a 2-μm-thick SiO$_2$ over cladding layer on top of the Si waveguide. The window region is opened in a straight section of the ring resonator. The window region was patterned by photolithography with AZ 5218 photoresist. The SiO$_2$ in the window region was removed using reactive ion etching (RIE) in CF$_4$ plasma, and the top surface of Si was completely exposed by wet etching with DHF. Finally, the CAFO/MgO films were deposited by sputtering under the optimized conditions described in Section 2. A optical microscopic picture of the fabricated device before CAFO deposition is shown in Fig. 5.

4. DEVICE CHARACTERIZATION

A fiber-device-fiber setup [38] was used to characterize the isolation performance of this device at telecom wavelengths by coupling TM-polarized light through a bus-line waveguide. Prior to the measurements, the CAFO film was magnetized in-plane and perpendicular to the direction of light propagation using an electromagnetic coil at 15 kOe for 5 min. As shown in Fig. 2(a), the applied magnetic field was sufficient to saturate the CAFO film. Once the magnetization is saturated, the CAFO provides the MO effect owing to the remnant magnetization in the absence of an external magnet.

The transmission spectra were measured in the clockwise (CW) and counterclockwise (CCW) directions along the ring resonator for TM-polarized light, as shown in Fig. 6. The green curve represents the straight waveguide used as a reference adjacent to the device. It can be observed that IR of 24.7 dB and insertion loss (IL) of 16.1 dB at a wavelength of 1549.5 nm were obtained between the two propagation directions under the self-biased CAFO film. The nonreciprocal resonant wavelength splitting ($\Delta\lambda$) can be written as

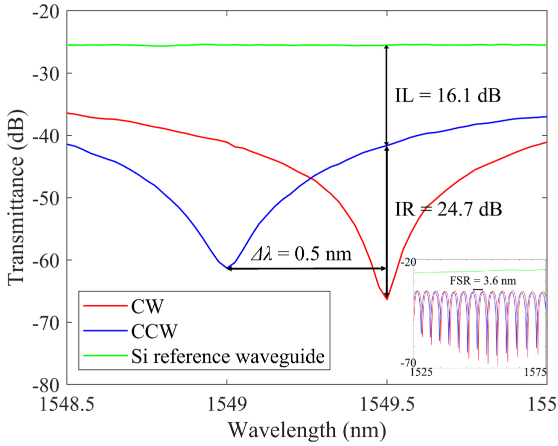

Fig. 6. Transmission spectra of the reference waveguide and the isolator in forward and backward transmission.

$$\Delta\lambda = \frac{\mathrm{FSR} \cdot L_{\mathrm{MO}} \cdot \mathrm{NRPS}_{\mathrm{TM}}}{2\pi}, \tag{4}$$

where the FSR is the free spectral range of the resonant peaks. The FSR and $\Delta\lambda$ in this device were 3.6 nm and 0.5 nm, respectively. Using Eq. (4), the experimental NRPS is 16.8 rad/mm, more than twice the theoretical NRPS of 6.1 rad/mm obtained using Eq. (2). The theoretical NRPS was based on the Faraday rotation coefficient of $-4{,}350$ deg/cm under in-plane remanent magnetization of as-deposited film, which was much less than that of $-15{,}000$ deg/cm under saturation magnetization. The CAFO/MgO film showed strong remanence for out-of-plane magnetization, as shown in Fig. 2(a); however, it could have strong remanence in the patterned CAFO film owing to shape anisotropy [39]. We presume the remanent Faraday rotation coefficient would be as much as $-12{,}000$ deg/cm. Regardless, this is an underestimation. The operation wavelength for the isolation peak can be

Table 2. Comparison of Device Performance at 1550 nm for Si-Based Isolator

Bias Magnet	Isolator Type	MO Material	Isolation Ratio (dB)	Insertion Loss (dB)	Footprint (μm x μm)	Reference
Needed	MZI	Ce:YIG	27	13	500 × 500	[24]
Needed	MZI (TM/TE)	Ce:YIG/YIG	30	59	940 × 330 870 × 340	[21]
Needed (electrical)	Ring	Ce:YIG	32	10	70 × 70	[23]
Needed	Ring	Ce:YIG/YIG	19.5	18.8	290	[25]
Needed	Faraday rotator	Ce:TbIG	30	7	7350 × 0.5	[22]
Free	Faraday rotator	BiIG	29	1.5	480 × 12	[20]
Free	Ring	CAFO	24.7	16.1	43 × 71	This work

tuned by integrating a thermo-optic phase shifter with a structure of low-power consumption [40].

Table 2 compares the device performance and footprint of Si-based optical isolators on silicon. Our device has a remarkably small footprint. The IR is sufficiently large for optical-isolator performance; however, a high IL remains an important issue. The loss breakdown included an absorption loss of ~10 dB in the CAFO region, a scattering loss of ~1 dB at the boundary of the CAFO region, and an insufficient resonant shift of ~5 dB. The absorption and scattering losses can be reduced slightly by increasing the thickness of the MgO buffer layer to reduce light confinement in the CAFO film. However, it should be noted that the NRPS is also reduced. If the absorption loss is half and the Faraday rotation coefficient under remanent magnetization is twice that of the current CAFO film, the IL of the isolator can be improved to less than 5 dB.

5. CONCLUSION

In summary, we experimentally demonstrated an ultra-compact TM mode optical isolator (43 × 71 μm^2) using deposited CAFO film as MO material, achieving the IR of 24.7 dB at a wavelength of 1549.5 nm. To the best of our knowledge, this is the smallest optical isolator reported thus far. The device was self-biased by the strong remanent magnetization of the CAFO film and did not require an external magnet. The high IL of 16.1 dB remains a challenge, but it can be solved by a little more improvement on lower absorption loss and larger θ_F of CAFO film. In other words, depositing a CAFO film with a larger FoM, including magnetic anisotropy, is key to improving the optical isolator properties. Then, CAFO supersedes conventional YIGs to realize compact and integrated optical isolators.

Funding. Japan Society for the Promotion of Science (22K18805, 23H04802); Core Research for Evolutional Science and Technology (JPMJCR18T4); New Energy and Industrial Technology Development Organization (JPNP16007, JPNP20004); Advanced Research Infrastructure for Materials and Nanotechnology in Japan (ARIM) (JPMXP1223IT0018, JPMXP1223IT0019).

Acknowledgment. This work was conducted at Nanofab, Tokyo Tech.

Disclosures. The authors declare no conflicts of interest.

Data availability. The data underlying the results presented in this paper are not publicly available at this time but may be obtained from the authors upon reasonable request.

REFERENCES

1. D. Jalas, A. Petrov, M. Eich, *et al.*, "What is—and what is not—an optical isolator," Nat. Photonics **7**, 579–582 (2013).
2. A. D. White, G. H. Ahn, K. V. Gasse, *et al.*, "Integrated passive nonlinear optical isolators," Nat. Photonics **17**, 143–149 (2023).
3. K. Y. Yang, J. Skarda, M. Cotrufo, *et al.*, "Inverse-designed non-reciprocal pulse router for chip-based LiDAR," Nat. Photonics **14**, 369–374 (2020).
4. K. Abdelsalam, T. Li, J. B. Khurgin, *et al.*, "Linear isolators using wavelength conversion," Optica **7**, 209–213 (2020).
5. L. Del Bino, J. M. Silver, M. T. M. Woodley, *et al.*, "Microresonator isolators and circulators based on the intrinsic nonreciprocity of the Kerr effect," Optica **5**, 279–282 (2018).
6. M. Krause, H. Renner, and E. Brinkmeyer, "Optical isolation in silicon waveguides based on nonreciprocal Raman amplification," Electron. Lett. **44**, 691–693 (2008).
7. M. Yu, R. Cheng, C. Reimer, *et al.*, "Integrated electro-optic isolator on thin-film lithium niobate," Nat. Photonics **17**, 666–671 (2023).
8. J. F. Herrmann, V. Ansari, J. Wang, *et al.*, "Mirror symmetric on-chip frequency circulation of light," Nat. Photonics **16**, 603–608 (2022).
9. N. Dostart, H. Gevorgyan, D. Onural, *et al.*, "Optical isolation using microring modulators," Opt. Lett. **46**, 460–463 (2021).
10. C. R. Doerr, L. Chen, and D. Vermeulen, "Silicon photonics broadband modulation-based isolator," Opt. Express **22**, 4493–4498 (2014).
11. Z. Yu and S. Fan, "Complete optical isolation created by indirect interband photonic transitions," Nat. Photonics **3**, 91–94 (2009).
12. D. B. Sohn, O. E. Örsel, and G. Bahl, "Electrically driven optical isolation through phonon-mediated photonic Autler–Townes splitting," Nat. Photonics **15**, 822–827 (2021).
13. C. J. Sarabalis, R. Van Laer, R. N. Patel, *et al.*, "Acousto-optic modulation of a wavelength-scale waveguide," Optica **8**, 477–483 (2021).
14. D. B. Sohn and G. Bahl, "Direction reconfigurable nonreciprocal acousto-optic modulator on chip," APL Photonics **4**, 126103 (2019).
15. A. Yu. Petrov, "Non-reciprocal modulation via acousto-optics," Nat. Photonics **12**, 570–571 (2018).
16. R. Fleury, D. L. Sounas, and A. Alù, "Non-reciprocal optical mirrors based on spatio-temporal acousto-optic modulation," J. Opt. **20**, 034007 (2018).
17. S. Liu, D. Minemura, and Y. Shoji, "Silicon-based integrated polarization-independent magneto-optical isolator," Optica **10**, 373–378 (2023).
18. M. A. Serrano-Núñez, Y. Shoji, and T. Mizumoto, "Small magnetless integrated optical isolator using a magnetized cobalt ferrite film," IEICE Electron. Express **19**, 20210500 (2022).
19. W. Yan, Y. Yang, S. Liu, *et al.*, "Waveguide-integrated high-performance magneto-optical isolators and circulators on silicon nitride platforms," Optica **7**, 1555–1562 (2020).
20. D. Karki, V. Stenger, A. Pollick, *et al.*, "Broadband bias-magnet-free on-chip optical isolators with integrated thin film polarizers," J. Lightwave Technol. **38**, 827–833 (2020).
21. Y. Zhang, Q. Du, C. Wang, *et al.*, "Monolithic integration of broadband optical isolators for polarization-diverse silicon photonics," Optica **6**, 473–478 (2019).
22. K. Srinivasan, C. Zhang, P. Dulal, *et al.*, "High-gyrotropy seedlayer-free Ce:TbIG for monolithic laser-matched SOI optical isolators," ACS Photonics **6**, 2455–2461 (2019).
23. P. Pintus, D. Huang, C. Zhang, *et al.*, "Microring-based optical isolator and circulator with integrated electromagnet for silicon photonics," J. Lightwave Technol. **35**, 1429–1437 (2017).

24. Y. Shoji, Y. Shirato, and T. Mizumoto, "Silicon Mach–Zehnder interferometer optical isolator having 8 nm bandwidth for over 20 dB isolation," Jpn. J. Appl. Phys. **53**, 022202 (2014).
25. L. Bi, J. Hu, P. Jiang, *et al.*, "On-chip optical isolation in monolithically integrated non-reciprocal optical resonators," Nat. Photonics **5**, 758–762 (2011).
26. Y. Shoji, T. Mizumoto, H. Yokoi, *et al.*, "Magneto-optical isolator with silicon waveguides fabricated by direct bonding," Appl. Phys. Lett. **92**, 071117 (2008).
27. Y. Kim, D. J. Bang, Y. Kim, *et al.*, "Magneto-optic property measurement of bismuth substituted yttrium iron garnet films prepared by metal-organic-decomposition method at the 1310-nm and 1550-nm wavelengths," J. Magn. Magn. Mater. **492**, 165673 (2019).
28. T. Shintaku, T. Uno, and M. Kobayashi, "Magneto-optic channel waveguides in Ce-substituted yttrium iron garnet," J. Magn. Magn. Mater. **74**, 4877–4881 (1993).
29. X. Y. Sun, Q. Du, T. Goto, *et al.*, "Single-step deposition of cerium-substituted yttrium iron garnet for monolithic on-chip optical isolation," ACS Photonics **2**, 856–863 (2015).
30. M. A. Serrano-Núñez, Y. Shoji, and T. Mizumoto, "Giant Faraday rotation of cobalt ferrite thin films deposited on silicon substrates for silicon photonic nonreciprocal device applications," Appl. Phys. Express **13**, 062002 (2020).
31. K. Suzuki, T. Namikawa, and Y. Yamazaki, "Preparation of zinc- and aluminum-substituted cobalt-ferrite thin films and their Faraday rotation," Jpn. J. Appl. Phys. **27**, 361 (1988).
32. M. Ning, J. Li, C. K. Ong, *et al.*, "High perpendicular coercive field of (100)-oriented $CoFe_2O_4$ thin films on Si (100) with MgO buffer layer," J. Appl. Phys. **103**, 013911 (2008).
33. N. A. Basit, H. K. Kim, and J. Blachere, "Growth of highly oriented Pb(Zr, Ti)O_3 films on MgO-buffered oxidized Si substrates and its application to ferroelectric nonvolatile memory field-effect transistors," Appl. Phys. Lett. **73**, 3941–3943 (1998).
34. Ü. Özgür, Y. I. Alivov, C. Liu, *et al.*, "A comprehensive review of ZnO materials and devices," J. Appl. Phys. **98**, 041301 (2005).
35. Y. Jiang, X. Li, X. Zhang, *et al.*, "Absence of auxeticity in $CoFe_2O_4$ epitaxial films," Jpn. J. Appl. Phys. **61**, 070901 (2022).
36. S. E. Shirsath, X. Liu, Y. Yasukawa, *et al.*, "Switching of magnetic easy-axis using crystal orientation for large perpendicular coercivity in $CoFe_2O_4$ thin film," Sci. Rep. **6**, 30074 (2016).
37. K. Ashida, M. Okano, M. Ohtsuka, *et al.*, "Ultrahigh-Q photonic crystal nanocavities fabricated by CMOS process technologies," Opt. Express **25**, 18165–18174 (2017).
38. E. Ishida, K. Miura, Y. Shoji, *et al.*, "Amorphous-Si waveguide on a garnet magneto-optical isolator with a TE mode nonreciprocal phase shift," Opt. Express **25**, 452–462 (2017).
39. H. Onoda, H. Sukegawa, and H. Yanagihara, "Study of induced magnetic anisotropy by lattice distortion in cobalt ferrite thin film grown on $(Mg,Sn)_3O_4$ buffer layers," IEEE Trans. Magn. **56**, 1–4 (2020).
40. P. Sun and R. M. Reano, "Submilliwatt thermo-optic switches using free-standing silicon-on-insulator strip waveguides," Opt. Express **18**, 8406–8411 (2010).